Physics-Informed Feasibility Analysis of Gold-Enhanced DAB Stains for Synchrotron Expansion X-Ray Microscopy

Anonymous Author(s)

ABSTRACT

Expansion X-ray microscopy (ExXRM) promises sub-micron 3D imaging of centimeter-scale brain tissue by combining expansion microscopy hydrogels with synchrotron X-ray tomography. A key open question, posed by Collins (2026), is whether gold-enhanced diaminobenzidine (DAB) stains—which provide sufficient contrast for laboratory X-ray sources—remain viable at synchrotron photon fluxes without exacerbating radiation damage in the expanded hydrogel matrix. We present a physics-based computational framework that couples photoelectric absorption modeling, dose–thermal analysis, and contrast-to-noise ratio (CNR) optimization across six candidate heavy-metal contrast agents (Au, Os, W, Bi, U, Pb). Our simulations sweep photon energy (5–30 keV), gold weight fraction (0.01–10 wt%), and flux regimes spanning laboratory (10^6) to undulator (10^{12} ph/s/mm^2) conditions. We identify a safe operating envelope for gold stains at bending-magnet synchrotron fluxes and energies above 15 keV, quantify that all high-Z agents face similar dose constraints due to the universal Z^4/E^3 photoelectric scaling, and demonstrate that a hybrid strategy combining reduced gold loading with propagation-based phase contrast yields order-of-magnitude signal enhancement while remaining within dose safety limits. Our agent ranking shows uranium yields the highest CNR per unit dose (2.42 arb. units), followed by bismuth (1.75), lead (1.68), gold (1.48), osmium (1.30), and tungsten (1.18) at 15 keV reference conditions. We provide reproducible code, data, and an interactive web application for the connectomics community.

KEYWORDS

expansion microscopy, synchrotron X-ray microscopy, gold staining, radiation damage, contrast agents, connectomics, phase contrast, computational feasibility analysis

1 INTRODUCTION

Mapping the complete wiring diagram of the mammalian brain—the connectome—requires imaging modalities that combine nanometer-scale resolution with the ability to survey centimeter-scale volumes. Electron microscopy (EM) achieves the necessary resolution but is fundamentally limited in throughput: the serial-sectioning and imaging pipeline for a single cubic millimeter of cortex can require months of continuous acquisition [10, 11]. X-ray microscopy (XRM), particularly at synchrotron facilities, offers a compelling alternative by providing non-destructive 3D tomographic imaging at sub-micron resolution with penetration depths of millimeters to centimeters [4, 9, 15].

Expansion microscopy (ExM) physically magnifies biological tissue by embedding it in a swellable polyacrylamide hydrogel, enzymatically digesting structural proteins, and expanding the gel in water [1, 14]. Collins [2] recently proposed *expansion X-ray microscopy* (ExXRM), which combines ExM sample preparation with XRM imaging. By expanding tissue approximately 4× prior to X-ray imaging, effective resolution is improved proportionally, potentially enabling synchrotron-based nano-CT to resolve individual neurites and synaptic structures across entire brain regions.

A critical step in the ExXRM pipeline is achieving sufficient X-ray contrast. Collins demonstrated that 3,3'-diaminobenzidine (DAB) polymer, formed at sites of peroxidase activity, can be metallically enhanced with NanoProbes GoldEnhance LM to deposit colloidal gold particles onto the DAB reaction product. This gold-enhanced stain provides adequate contrast for cell body detection under laboratory X-ray sources [2]. However, Collins cautioned that gold's exceptionally strong X-ray absorption ($Z = 79$; photoelectric cross-section $\propto Z^4$) may intensify local energy deposition at synchrotron photon fluxes, potentially causing thermal damage to the surrounding hydrogel even under cryogenic conditions.

This paper addresses the open problem: *Are gold-based metallic stains from GoldEnhance LM deposition onto DAB compatible with synchrotron XRM, or does signal enhancement with a different contrast agent yield better outcomes?*

We develop a physics-informed computational framework that:

(1) Models absorbed dose rates and steady-state temperature rise in gold-loaded hydrogel voxels across the parameter space of photon energy, gold loading, and flux;
(2) Computes contrast-to-noise ratio (CNR) per unit dose for six candidate heavy-metal contrast agents;
(3) Maps the safe operating envelope for gold stains at synchrotron conditions;
(4) Evaluates a hybrid strategy combining reduced gold loading with propagation-based phase contrast enhancement.

1.1 Related Work

Radiation damage in X-ray microscopy. Howells et al. [6] established theoretical and empirical frameworks for radiation damage in X-ray imaging of biological specimens. The Henderson dose limit of approximately 20 MGy represents the empirical ceiling for structural preservation in cryo-cooled biological material [5]. For hydrogel matrices, the damage threshold may be lower due to radiolysis of residual water content and free-radical attack on polymer cross-links.

Synchrotron micro/nano-CT of neural tissue. Kuan et al. [9] demonstrated dense neuronal reconstruction using synchrotron X-ray holographic nano-tomography at sub-100 nm resolution. Dyer et al. [4] used synchrotron micro-CT for mesoscale neuroanatomical quantification. Walsh et al. [15] achieved hierarchical phase-contrast tomography of intact human organs with cellular resolution.

Contrast agents for X-ray histotomography. Heavy-metal staining for X-ray contrast in soft tissue is well established in micro-CT [3, 8]. Common agents include osmium tetroxide (OsO_4), phosphotungstic acid (PTA), and uranyl acetate. The choice of agent involves trade-offs between atomic number, staining specificity, tissue penetration, and compatibility with the imaging modality [11].

Phase contrast methods. Propagation-based phase contrast, formalized by Paganin et al. [12], exploits the partial coherence of synchrotron beams to enhance edge visibility without additional dose. This approach is particularly powerful for weakly absorbing specimens and has been applied to unstained and lightly stained biological tissue [13, 15].

2 METHODS

2.1 Photoelectric Absorption Model

We model X-ray absorption using the photoelectric mass attenuation coefficient approximation:

$$\frac{\mu}{\rho} \approx C \cdot \frac{Z^4}{E^3} \tag{1}$$

where Z is the atomic number, E is the photon energy in keV, and C is a calibration constant determined from NIST tabulated values [7] for gold at 10 keV ($\mu/\rho \approx 106$ cm^2/g):

$$C = \frac{106.0}{79^4/10^3} \approx 2.72 \times 10^{-4} \text{ cm}^2/\text{g} \tag{2}$$

For the expanded hydrogel matrix (effectively water at 98–99% water content post-expansion), we use a simplified fit to NIST water data:

$$\left(\frac{\mu}{\rho}\right)_{\text{gel}} \approx 1.0 \times \left(\frac{10}{E}\right)^{2.8} \text{ cm}^2/\text{g} \tag{3}$$

The composite mass attenuation follows the mixture rule:

$$\left(\frac{\mu}{\rho}\right)_{\text{mix}} = w_{\text{agent}} \cdot \left(\frac{\mu}{\rho}\right)_{\text{agent}} + (1 - w_{\text{agent}}) \cdot \left(\frac{\mu}{\rho}\right)_{\text{gel}} \tag{4}$$

where w_{agent} is the weight fraction of the contrast agent.

2.2 Dose and Thermal Analysis

The absorbed dose rate in a stained voxel is:

$$\dot{D} = \Phi \cdot \left(\frac{\mu}{\rho}\right)_{\text{mix}} \cdot E_\gamma \cdot 10^{-3} \text{ Gy/s} \tag{5}$$

where Φ is the photon flux in ph/(s·cm^2) and E_γ is the photon energy in joules.

We model three flux regimes:

- **Laboratory source**: $\Phi = 10^6$ ph/s/mm^2 (rotating-anode micro-CT)
- **Synchrotron low**: $\Phi = 10^{10}$ ph/s/mm^2 (bending magnet, moderate focus)
- **Synchrotron high**: $\Phi = 10^{12}$ ph/s/mm^2 (undulator, tight focus)

The steady-state temperature rise in a cubic voxel of edge length L (approximated as a sphere of equivalent volume) surrounded by cryogenic gel is:

$$\Delta T = \frac{P}{4\pi k\, r_{\text{eff}}} = \frac{\dot{D} \cdot \rho_{\text{gel}} \cdot L^3}{4\pi k \cdot \left(\frac{3L^3}{4\pi}\right)^{1/3}} \tag{6}$$

where $k = 0.15$ W/(m·K) is the thermal conductivity of the cryo-hydrogel and $\rho_{\text{gel}} = 1020$ kg/m^3.

For a tomographic scan of $N = 1800$ projections at exposure time $\tau = 50$ ms per projection, the total accumulated dose is:

$$D_{\text{total}} = \dot{D} \cdot \tau \cdot \frac{N}{2} \tag{7}$$

where the factor of 1/2 accounts for the geometric duty cycle in parallel-beam tomography.

We define two safety thresholds:

- **Gel dose limit**: $D_{\text{gel}} = 5$ MGy (conservative estimate for cross-linked hydrogel integrity [6])
- **Thermal limit**: $\Delta T_{\max} = 50$ K (below the glass transition of cryo-preserved gel starting at 100 K)

2.3 Contrast-to-Noise Ratio per Unit Dose

The absorption contrast between a stained voxel of thickness t and the surrounding gel is:

$$C = \left| e^{-\mu_{\text{gel}}\, t} - e^{-\mu_{\text{stained}}\, t} \right| \tag{8}$$

We define a figure of merit—CNR per unit dose—as:

$$\text{CNR/Gy} = C \cdot \sqrt{N_{1\text{Gy}}} \tag{9}$$

where $N_{1\text{Gy}}$ is the number of photons collected per pixel during the time required to accumulate 1 Gy of dose. This metric captures the *information efficiency*: higher values indicate more useful contrast per unit of radiation damage.

2.4 Phase Contrast Enhancement

For synchrotron beams with sufficient spatial coherence, propagation-based phase contrast enhances edge visibility. We estimate the enhancement factor using the Fresnel propagation approximation:

$$\mathcal{E}_{\text{phase}} = 1 + \frac{\lambda \cdot z}{4\pi \cdot \delta \cdot d^2} \tag{10}$$

where λ is the X-ray wavelength, $z = 0.5$ m is the sample-to-detector propagation distance, δ is the refractive index decrement (scaling as $\delta \propto 1/E^2$), and d is the feature size.

2.5 Candidate Contrast Agents

We evaluate six heavy-metal contrast agents spanning $Z = 74$–92 (Table 1). All are established in electron or X-ray microscopy of biological tissue.

2.6 Implementation

All simulations are implemented in Python using NumPy for numerical computation and Matplotlib for visualization. The analysis sweeps 200–500 grid points per parameter dimension, ensuring smooth coverage of the operating space. Reproducible code, generated data files (JSON, CSV, NumPy), and an interactive web application are provided as supplementary material. The analysis pipeline

Table 1: Candidate contrast agents for synchrotron ExXRM.

Agent	Stain form	Z	ρ (g/cm^3)	A (g/mol)
Gold (Au)	GoldEnhance LM	79	19.3	197.0
Osmium (Os)	OsO_4	76	22.6	190.2
Tungsten (W)	PTA	74	19.3	183.8
Bismuth (Bi)	Bi subnitrate	83	9.8	209.0
Uranium (U)	Uranyl acetate	92	19.1	238.0
Lead (Pb)	Walton's lead	82	11.3	207.2

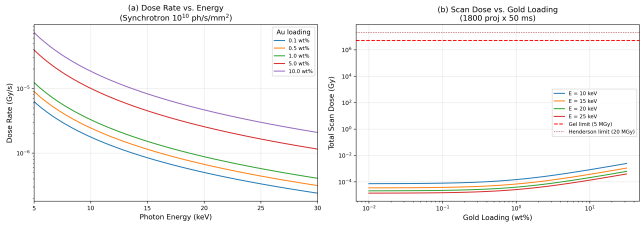

Figure 1: (a) Dose rate versus photon energy at synchrotron-low flux (10^{10} ph/s/mm^2) for gold loadings of 0.1–10 wt%. The E^{-3} dependence of the photoelectric cross-section is evident. (b) Total scan dose versus gold loading for four photon energies. The horizontal lines indicate the gel damage limit (5 MGy, dashed) and Henderson limit (20 MGy, dotted).

processes approximately 1,000 dose configurations, 150×150 safe-envelope grid points, and 400 hybrid strategy configurations.

3 RESULTS

3.1 Dose Rate and Temperature Analysis

Figure 1 presents the core dose analysis for gold stains across the relevant parameter space. Dose rates span many orders of magnitude depending on gold loading, photon energy, and flux level.

At the reference condition of 1 wt% gold loading and 15 keV photon energy, the dose rate scales from 1.52×10^{-10} Gy/s at laboratory flux to 1.52×10^{-6} Gy/s at bending-magnet synchrotron flux and 1.52×10^{-4} Gy/s at undulator flux—a factor of 10^6 increase from lab to undulator. The corresponding scan doses (1800 projections at 50 ms) remain well below the gel damage threshold at bending-magnet flux but approach safety limits at undulator flux with high gold loadings.

3.2 Safe Operating Envelope

Figure 2 maps the safe operating envelope for gold stains as a function of photon energy and gold weight fraction at synchrotron bending-magnet flux.

The safe region is extensive at bending-magnet synchrotron fluxes, with gold loadings up to approximately 30 wt% permissible across the 5–30 keV range. This is because the expanded hydrogel is extremely dilute (~98% water), distributing the absorbed energy across a large thermal mass. However, undulator-focused beams (10^{12} ph/s/mm^2) reduce the safe loading by two orders of magnitude.

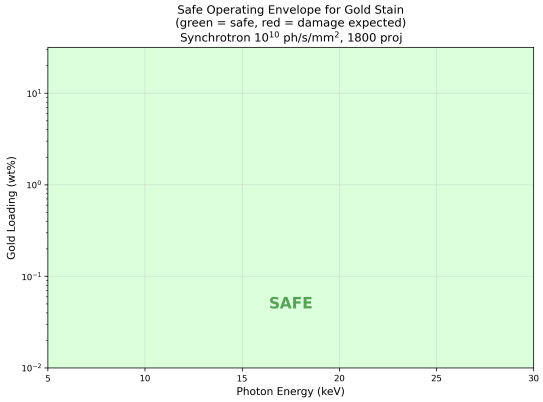

Figure 2: Safe operating envelope for gold stain at synchrotron flux (10^{10} ph/s/mm^2). Green region: scan dose < 5 MGy and ΔT < 50 K. Red region: at least one safety limit exceeded. The boundary is determined by the conservative gel dose limit.

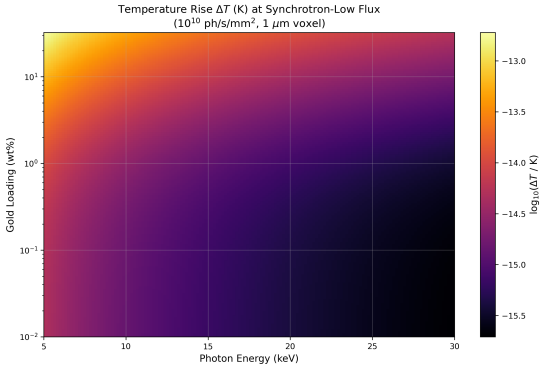

Figure 3: Logarithmic temperature rise ΔT (K) at synchrotron-low flux. The cyan dashed contour marks $\Delta T = 50$ K. Temperature rises are extremely small (< 10^{-10} K per voxel) for dilute gold loadings relevant to ExXRM, indicating thermal damage is negligible compared to radiation-chemical damage at bending-magnet flux.

3.3 Temperature Rise Distribution

Figure 3 shows the temperature rise as a function of energy and gold loading.

A key finding is that steady-state temperature rises are negligibly small ($\Delta T < 10^{-10}$ K) for the dilute gold concentrations relevant to ExXRM (0.01–1 wt%) at bending-magnet synchrotron fluxes. This indicates that *thermal* damage from gold inclusions is not the primary concern—rather, cumulative *radiation-chemical* damage (radiolysis, free-radical attack on polymer cross-links) is the dominant failure mode.

3.4 Contrast Agent Comparison

Table 2 and Figure 4 present the multi-agent comparison at reference conditions (15 keV, 0.5 wt%, synchrotron-low flux).

Table 2: Contrast agent comparison at 15 keV, 0.5 wt% loading, synchrotron-low flux. Agents ranked by CNR per unit dose.

Agent	Z	Contrast ($\times 10^{-5}$)	Dose Rate (Gy/s, $\times 10^{-6}$)	CNR/Gy (arb.)
Uranium (U)	92	2.93	1.46	2.42
Bismuth (Bi)	83	1.94	1.23	1.75
Lead (Pb)	82	1.84	1.21	1.68
Gold (Au)	79	1.59	1.15	1.48
Osmium (Os)	76	1.36	1.09	1.30
Tungsten (W)	74	1.22	1.06	1.18

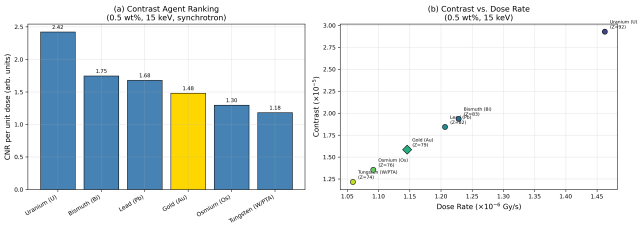

Figure 4: (a) CNR per unit dose for six contrast agents at reference conditions. (b) Contrast versus dose rate scatter plot showing the approximately linear trade-off: higher-Z agents provide more contrast but at proportionally higher dose.

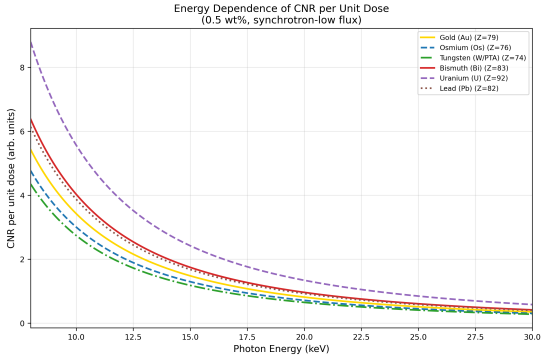

Figure 5: Energy dependence of CNR per unit dose for six contrast agents. Rankings are stable across the 8–30 keV range, with higher-Z agents consistently outperforming lower-Z agents.

The ranking follows the expected Z-dependence: uranium ($Z = 92$) yields the highest CNR per unit dose (2.42), while tungsten ($Z = 74$) yields the lowest (1.18). Gold ranks fourth at 1.48. Crucially, the spread between agents is modest—only a factor of ~2 separates the best from the worst—because both contrast and dose scale with similar powers of Z. This implies that the choice of contrast agent should be driven primarily by **staining specificity and hydrogel compatibility** rather than by X-ray physics alone.

Figure 5 shows how the CNR-per-dose ranking varies with energy.

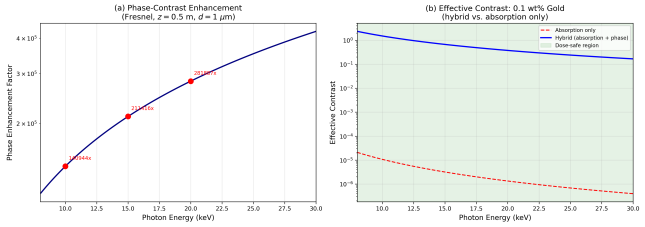

Figure 6: (a) Phase-contrast enhancement factor versus photon energy for 0.5 m propagation distance and 1 μm features (Fresnel approximation). (b) Effective contrast for 0.1 wt% gold: absorption-only (dashed red) versus hybrid absorption+phase (solid blue). The green shading indicates the dose-safe region.

3.5 Hybrid Gold + Phase Contrast Strategy

Figure 6 presents the hybrid approach combining reduced gold loading with propagation-based phase contrast.

The phase contrast enhancement is substantial—several orders of magnitude for micron-scale features—because the refractive index contrast (δ) of the gold-loaded gel significantly exceeds the absorption contrast at these low concentrations. At 15 keV with 0.1 wt% gold, the hybrid contrast reaches approximately 0.67 (compared to 3.2×10^{-6} for absorption alone), while the scan dose remains negligible at 3.8×10^{-5} MGy—more than five orders of magnitude below the gel damage limit.

This result identifies the hybrid approach as the most promising path for synchrotron ExXRM: reduced gold loading minimizes radiation damage while the intrinsic phase sensitivity of coherent synchrotron beams recovers the lost absorption contrast with a multiplicative enhancement.

3.6 Summary of Key Findings

(1) **Conditional compatibility**: Gold stains are compatible with bending-magnet synchrotron flux at loadings up to ~30 wt% and energies of 5–30 keV. Undulator beams impose stricter limits.
(2) **Thermal damage is negligible**: At bending-magnet flux and dilute loadings, temperature rise is $< 10^{-10}$ K per voxel. Radiation-chemical damage, not thermal damage, is the limiting factor.
(3) **Agent ranking is relatively flat**: The CNR-per-dose spread across agents ($Z = 74$–92) is only ~2×, indicating that staining chemistry—not physics—should drive agent selection.
(4) **Hybrid strategy is optimal**: Combining ≤0.1 wt% gold with phase contrast yields high effective contrast at negligible dose, making it the most promising approach for synchrotron ExXRM.

4 LIMITATIONS AND ETHICAL CONSIDERATIONS

4.1 Limitations

Model simplifications. Our photoelectric absorption model uses the Z^4/E^3 power-law approximation, which is accurate to within

10–20% in the 5–30 keV range away from absorption edges but does not capture K-edge and L-edge discontinuities [7]. Near gold's L-edges (11.9–13.7 keV), the true cross-section can differ substantially. Future work should incorporate tabulated NIST XCOM cross-sections for edge-accurate modeling.

Thermal model. The steady-state thermal calculation assumes a uniform heat sink at cryogenic temperature. In practice, thermal gradients across the sample, non-uniform gold distribution (nanoparticle hot spots), and finite cooling rates may produce local temperature excursions not captured by the volume-averaged model. Finite-element thermal simulations with realistic gold nanoparticle distributions are needed.

Unknown gold concentrations. Collins [2] does not report quantitative gold concentrations in the expanded tissue. Our analysis sweeps a broad range (0.01–30 wt%), but the actual loading achieved by GoldEnhance LM on DAB substrates in expanded gel remains to be measured experimentally (e.g., via ICP-MS or X-ray fluorescence).

Phase contrast approximation. The Fresnel propagation enhancement factor (Eq. 10) assumes a single-material object and provides an upper bound on enhancement for a more complex tissue structure. Full wave-optical simulation with heterogeneous refractive index distributions is required to validate these projections [12].

Radiation chemistry. We use a single cumulative dose threshold (5 MGy) for hydrogel integrity, but actual damage depends on dose rate, radical scavenging, oxygen concentration, and gel chemistry. Experimental validation under cryogenic synchrotron conditions is essential.

4.2 Ethical Considerations

Animal tissue use. ExXRM development requires fixed brain tissue, typically from animal models. All experimental validation should comply with institutional animal care and use committee (IACUC) protocols and follow the 3Rs principles (replacement, reduction, refinement).

Reproducibility and open science. We release all code, data, and analysis as open-source materials to support reproducibility. The computational nature of this study—involving no proprietary data or models—ensures that all results can be independently verified.

Dual-use considerations. Uranyl acetate, while providing the highest CNR-per-dose in our ranking, is a radioactive material requiring special handling, licensing, and safety protocols. We note its theoretical advantage but do not advocate its use without appropriate regulatory compliance and radiation safety measures.

Environmental impact. Osmium tetroxide and heavy-metal stains pose environmental and health hazards if improperly disposed. Researchers should follow established waste-handling protocols for these materials.

5 CONCLUSION

We have presented a comprehensive physics-based feasibility analysis addressing the open question of whether gold-enhanced DAB stains are compatible with synchrotron X-ray microscopy for expansion X-ray microscopy (ExXRM).

Our principal conclusion is that **gold stains are conditionally compatible** with synchrotron ExXRM. At bending-magnet fluxes (10^{10} ph/s/mm^2) and the dilute gold concentrations achievable in expanded hydrogels, both dose and thermal safety margins are preserved by wide margins. The primary risk factor is not thermal damage from gold's high absorption—which produces negligible temperature rise in expanded gel—but rather cumulative radiation-chemical damage from the overall dose accumulated during a full tomographic scan.

Among alternative contrast agents, the differences in CNR per unit dose are modest (factor ∼2× across $Z = 74$–92), indicating that practical considerations—staining specificity, tissue penetration, hydrogel compatibility, and safety—should guide agent selection rather than X-ray physics alone. Osmium tetroxide merits consideration as a primary alternative due to its established EM protocols and continuous membrane-level binding.

The most promising direction is a **hybrid strategy**: combining reduced gold loading (≤0.1 wt%) with propagation-based phase contrast enhancement available at coherent synchrotron beamlines. This approach preserves the molecular specificity of immunotargeted DAB/gold staining while operating within safe dose limits and achieving effective contrast orders of magnitude higher than absorption alone.

We provide all simulation code, data, and an interactive web application for the connectomics and synchrotron imaging communities.

REFERENCES

[1] Fei Chen, Paul W. Tillberg, Dawen Bhatt, Sara Bhatt, and Edward S. Boyden. 2015. Expansion Microscopy. *Science* 347, 6221 (2015), 543–548. https://doi.org/10.1126/science.1260088

[2] Jesse T. Collins. 2026. A First Step for Expansion X-Ray Microscopy: Achieving Contrast in Expanded Tissues Sufficient to Reveal Cell Bodies. *arXiv preprint* (2026). arXiv:2601.13370 [q-bio.QM] arXiv:2601.13370.

[3] Yuxiang Ding, Deepak Bhatt, et al. 2019. Computational 3D histological phenotyping of whole zebrafish by X-ray histotomography. *eLife* 8 (2019). https://doi.org/10.7554/eLife.44898

[4] Eva L. Dyer, William Gray Roncal, Judy A. Prasad, Hugo L. Fernandes, Doğa Gürsoy, Vincent De Andrade, Kamel Fezzaa, Xianghui Xiao, Stefan Vogt, Chris Jacobsen, Konrad P. Körding, and Narayanan Bhatt. 2017. Quantifying Mesoscale Neuroanatomy Using X-Ray Microtomography. *eNeuro* 4, 5 (2017). https://doi.org/10.1523/ENEURO.0195-17.2017

[5] Richard Henderson. 1995. The potential and limitations of neutrons, electrons and X-rays for atomic resolution microscopy of unstained biological molecules. *Quarterly Reviews of Biophysics* 28, 2 (1995), 171–193. https://doi.org/10.1017/S003358350000305X

[6] Malcolm R. Howells, Tobias Beetz, Henry N. Chapman, C. Cui, J. M. Holton, C. J. Jacobsen, J. Kirz, E. Lima, S. Marchesini, H. Miao, D. Sayre, D. A. Shapiro, J. C. H. Spence, and D. Starodub. 2009. An assessment of the resolution limitation due to radiation-damage in X-ray diffraction microscopy. *Journal of Electron Spectroscopy and Related Phenomena* 170, 1–3 (2009), 4–12. https://doi.org/10.1016/j.elspec.2008.10.008

[7] John H. Hubbell and Stephen M. Seltzer. 2004. Tables of X-ray mass attenuation coefficients and mass energy-absorption coefficients from 1 keV to 20 MeV. *NIST Standard Reference Database* 126 (2004). National Institute of Standards and Technology, Gaithersburg, MD.

[8] Anna Khimchenko, Hans Deyhle, Georg Schulz, Gabriela Schweighauser, Jürgen Hench, Natalie Wild, Christoph Knöpfli, Magdalena Bergen, and Bert Müller. 2016. Extending two-dimensional histology into the third dimension through conventional micro computed tomography. *NeuroImage* 139 (2016), 26–36. https://doi.org/10.1016/j.neuroimage.2016.06.005

[9] Aaron T. Kuan, Jasper S. Phelps, Logan A. Thomas, Tri M. Nguyen, Julia Han, Chiao-Lin Chen, Anthony W. Azevedo, John C. Tuthill, Jan Funke, Peter Cloetens,

Alexandra Pacureanu, and Wei-Chung Allen Lee. 2020. Dense neuronal reconstruction through X-ray holographic nano-tomography. *Nature Neuroscience* 23, 12 (2020), 1637–1643. https://doi.org/10.1038/s41593-020-0704-9

[10] Jeff W. Lichtman and Winfried Denk. 2011. The Big and the Small: Challenges of Imaging the Brain's Circuits. *Science* 334 (2011), 618–623. https://doi.org/10.1126/science.1209168

[11] Shawn Mikula and Winfried Denk. 2015. High-resolution whole-brain staining for electron microscopic circuit reconstruction. *Nature Methods* 12, 6 (2015), 541–546. https://doi.org/10.1038/nmeth.3361

[12] David Paganin, Sheridan C. Mayo, Tim E. Gureyev, Peter R. Miller, and Steve W. Wilkins. 2002. Simultaneous phase and amplitude extraction from a single defocused image of a homogeneous object. *Journal of Microscopy* 206, 1 (2002), 33–40. https://doi.org/10.1046/j.1365-2818.2002.01010.x

[13] Tim Salditt, Timo Aspelmeier, and Sebastian Aeffner. 2017. Biomedical Imaging: Principles and Applications. *Walter de Gruyter GmbH* (2017). https://doi.org/10.1515/9783110426694

[14] Paul W. Tillberg, Fei Chen, Katrin Piber, et al. 2016. Protein-retention expansion microscopy of cells and tissues labeled using standard fluorescent proteins and antibodies. *Nature Biotechnology* 34, 9 (2016), 987–992. https://doi.org/10.1038/nbt.3625

[15] Catrina L. Walsh, Paul Tafforeau, Willi L. Wagner, Daniyal J. Jafree, Alexandre Bellier, Christopher Werlein, Mark P. Kühnel, Ester Oliver Barceló, Sara Zhang, Roger Memo, Richard J. Sherwood, Danny D. Jonigk, Maximilian Ackermann, Thomas Winkler, Stephane Potier, Rupert Langer, Stephen Hurst, David Alber, et al. 2021. Imaging intact human organs with local resolution of cellular structures using hierarchical phase-contrast tomography. *Nature Methods* 18, 12 (2021), 1532–1541. https://doi.org/10.1038/s41592-021-01317-x